Journal of Wind Engineering & Industrial Aerodynamics 253 (2024) 105831

Contents lists available at ScienceDirect

Journal of Wind Engineering & Industrial Aerodynamics

journal homepage: www.elsevier.com/locate/jweia

The role of Permeable Double Skin Façades on the onset of VIV on high-rise buildings

Marcello Catania *, Giulia Pomaranzi, Alberto Zasso

Politecnico di Milano - Department of Mechanical Engineering, Via G. La Masa 1, 20156, Milan, Italy

ARTICLE INFO

Keywords:
Porous Double Screen Façades
Vortex-induced vibrations
VIV
Rectangular cylinder
Wind tunnel testing

ABSTRACT

The application of stand-alone permeable screens for the mitigation of vortex shedding problems is a well-known option in wind engineering, usually adopted for bridges. Nevertheless, their employment in buildings is still in its early stages. Porous coverings are employed for aesthetic reasons and, recently, also for their capability to reduce the energetic impact of the building. Within this framework, the Permeable Double Screen Façades (PDSFs) are becoming popular in the architectural trends, but their effects on the building's aerodynamics are still an open topic. Specifically, it is still unclear which could be the role of the permeable layer on the vortex shedding mechanism, which currently represents one of the main design issues for tall and super tall buildings. The present study proposes an experimental investigation of the role of the PDSF in the vortex-induced vibrations (VIVs) of a prismatic building model with an aspect ratio $B/D = 3.33$. A semi-aeroelastic model of the building is tested for different Scruton numbers and a comparison between the PDSF and the solid façade case is proposed. Results highlight that the effectiveness of the PDSF in structural response mitigation appears to be dependent on the Scruton number and a threshold over which the PDSF successfully mitigates the onset of VIV is found.

1. Introduction

The Permeable Double Screen Façade (PDSF) is a multilayer cladding system characterized by an outer porous screen installed over the building's solid façade, creating a gap for air recirculation. Due to its capacity to improve the building's energy performance (Darkwa et al., 2014), this system has been adopted by architects in various recent projects (Fig. 1). When it comes to building design, as the PDSF system is directly exposed to environmental actions, it requires an accurate assessment of wind loading. Compared to the single façade case, the interaction of wind with a PDSF presents several unique challenges, which have received limited attention from the scientific community. The presence of an outer porous façade in the cladding system is expected to alter the aerodynamic behavior of a building when compared to a single-layer façade, affecting both cladding and structural design. Previous studies (Pomaranzi et al., 2020, 2021) have demonstrated that the porous layer can reduce pressure distribution on the inner façade by up to 50% compared to the single-layer scenario. Moreover, it has been observed that the permeable screen can induce modifications in the separated flow region (Pomaranzi et al., 2022b). This raises questions about the vortex shedding (VS) phenomenon, which is strongly dependent on the behavior of separated shear layers from the leading edges (Teimourian and Teimourian, 2021).

Therefore, this study aims to experimentally investigate the role that the PDSF plays in vortex shedding in a prismatic model representative of a high-rise building. We conduct a parametric investigation of the structural response to VS at different values of the mass-damping coefficients (Scruton number) and provide a comparative analysis between the single-layer façade and the PDSF to highlight the modifications induced by the porous layer.

1.1. Vortex-induced vibrations

Vortex-induced vibration (VIV) is a complex non-linear phenomenon resulting from the interaction between a moving fluid and an elastic body. It occurs when the transverse force caused by vortex shedding resonates with one of the structure's vibration modes.

Historically, this phenomenon was first investigated for cylindrical structures, such as pipes, cables, chimneys, and towers, due to their wide range of civil and technical applications (Giosan and Eng, 2013; Wang and yan Fan, 2019; Jafari et al., 2020). A comprehensive understanding of VIV mechanisms, especially for cylindrical structures, can be found in King (1977), Pantazopoulos (1994), Sarpkaya (2004), Williamson and Govardhan (2008).

* Corresponding author.
E-mail addresses: marcello.catania@polimi.it (M. Catania), giulia.pomaranzi@polimi.it (G. Pomaranzi), alberto.zasso@polimi.it (A. Zasso).

https://doi.org/10.1016/j.jweia.2024.105831
Received 2 November 2023; Received in revised form 25 June 2024; Accepted 13 July 2024
Available online 7 August 2024

Nomenclature		
D	[m]	Cross-wind dimension of the model (short edge)
B	[m]	Along-wind dimension of the model (long edge)
H	[m]	Height of the model
f_1	[Hz]	Natural frequency of the cross-wind vibration mode evaluated in still-air
f	[Hz]	Vortex-shedding frequency
ω_1, ω	[rad/s]	Corresponding circular frequencies ($\omega = 2\pi f$)
ξ_1	[–]	Adimensional damping of the cross-wind vibration mode $\left(\xi_1 = \frac{r_1}{2m_1\omega_1}\right)$
m_1	[kg/m]	Equivalent modal mass per unit length of the cross-wind vibration mode $\left(m_1 = 3\frac{J_1}{H^3}\right)$
J_1	[kg m^2]	Modal moment of inertia of the cross-wind vibration mode
t	[s]	Time
$x(t)$	[m]	Cross-wind top displacement amplitude
$F_{x,i}(t)$	[N]	Instantaneous cross-wind force amplitude, obtained as the integral of the pressure signals on the ith floor where i = 1 (top floor) and i = 8 (bottom floor)
$F_x(t)$	[N]	Instantaneous cross-wind force amplitude, obtained as the integral of the pressure signals along the height
$C_{F_x}(t)$	[–]	Cross-wind force coefficient $\left(C_F(t) = \frac{F_x(t)}{1/2\rho BHU^2}\right)$
F_{x1}	[N]	Amplitude of the first harmonic of the cross-wind force $\left(F_{x1} = \left\lvert \frac{1}{T_1}\int_{-T_1/2}^{T_1/2} F_x(t)e^{j\omega_1 t}dt \right\rvert\right)$
$C_{F_x,1}$	[–]	Amplitude of the first harmonic of the cross-wind force coefficient $\left(C_{F_x,1} = \frac{F_{x1}}{1/2\rho BHU^2}\right)$
ϕ_{x1}	[rad]	Phase of the first harmonic of cross-wind top displacement ($x(t) = x_1 sin(\omega_1 t + \phi_{x1})$)
$\phi_{F,1}$	[rad]	Phase of the VS component of the cross-wind force
$\Delta\phi_1$	[rad]	Phase difference between displacement and force in the cross-wind direction
U	[m/s]	Free stream velocity
U_{cr}	[m/s]	Critical free stream velocity of vortex resonance $(U_{cr} = f_1 D/St)$
ρ	[kg/m^3]	Air density
μ	[m^2/s]	Air kinematic viscosity
x_n	[–]	Non-dimensional top displacement ($x_n = x/D$)
U_n	[–]	Reduced wind speed ($U_n = U/U_{cr}$)
t_n	[–]	Reduced time (number of periods) ($t_n = tf_1$)
f_n	[Hz]	Reduced vortex-shedding frequency ($f_n = f/f_1$)
β	[–]	Porosity, ratio between empty and solid surface
k	[–]	Pressure lost coefficient $\left(k = \frac{\Delta p}{1/2\rho U^2}\right)$
d	[m]	Distance between the façade and the porous mesh
St	[–]	Strouhal number ($St = fD/U$)
Sc	[–]	Scruton number $\left(Sc = \frac{2\pi m_1 \xi_1}{\rho BD}\right)$
Re	[–]	Reynolds number $\left(Re = \frac{\rho UD}{\mu}\right)$

In this study, we focus on rectangular cylinders, whose geometry is characterized by edges that serve as permanent shear layer separation points. At the leading edge, the unstable detached shear layer generates vortical structures that interact with the body surface or the wake, subjecting the structure to periodic loading (Komatsu and Kobayashi, 1980). In elongated cylinders ($B/D > 4$), these motion-induced vortices move downstream at approximately 60% of the incoming wind velocity (Holmes and Bekele, 2020). They may interfere with the Karman vortices generated in the recirculating flow region at the trailing edge (Nguyen et al., 2018; Nakamura et al., 1991). For structures with aspect ratios between 2.8 and 6, both phenomena play a significant role in generating motion (Shiraishi and Matsumoto, 1983; Matsumoto et al., 1993). These vortices can trigger other instabilities, such as torsional flutter (Matsumoto, 1996; Matsumoto et al., 1996, 2005, 2008; Noda et al., 2003; Bartoli and Righi, 2006; Haan and Kareem, 2009) or divergent vibrations due to the coupling of VIV and galloping (Corless and Parkinson, 1988; Parkinson, 1989; Deniz and Staubli, 1997; Hémon and Santi, 2002; Tamura and Dias, 2003; Mannini et al., 2015). Cylinders with aspect ratios $B/D < 4$ are considered critical because the reattachment point of the separated flow can vary, especially in cross-sections close to unity ($1 < B/D < 1.5$). Increasing the Scruton number can separate the critical instability velocity well above the strouhal frequency, thus avoiding the coupling between VIV and galloping (Mannini et al., 2014).

The current research aims to deepen our understanding of cylinders with an aspect ratio of B/D = 3.33, which falls near the critical point.

1.2. VIV mitigation strategies

In the context of tall building design, it is required to study strategies for VIV mitigation. This phenomenon, if not properly addressed, can result in discomfort, motion sickness (Lamb and Kwok, 2017; Micheli et al., 2020), and even structural damage (Micheli et al., 2020, 2019; Samali et al., 2014; Vega and Konz, 2009). It is well known that increasing a structure's ability to dissipate energy is essential for reducing oscillation amplitudes. Proposed solutions typically involve adding equivalent damping to the system, either through active elements like

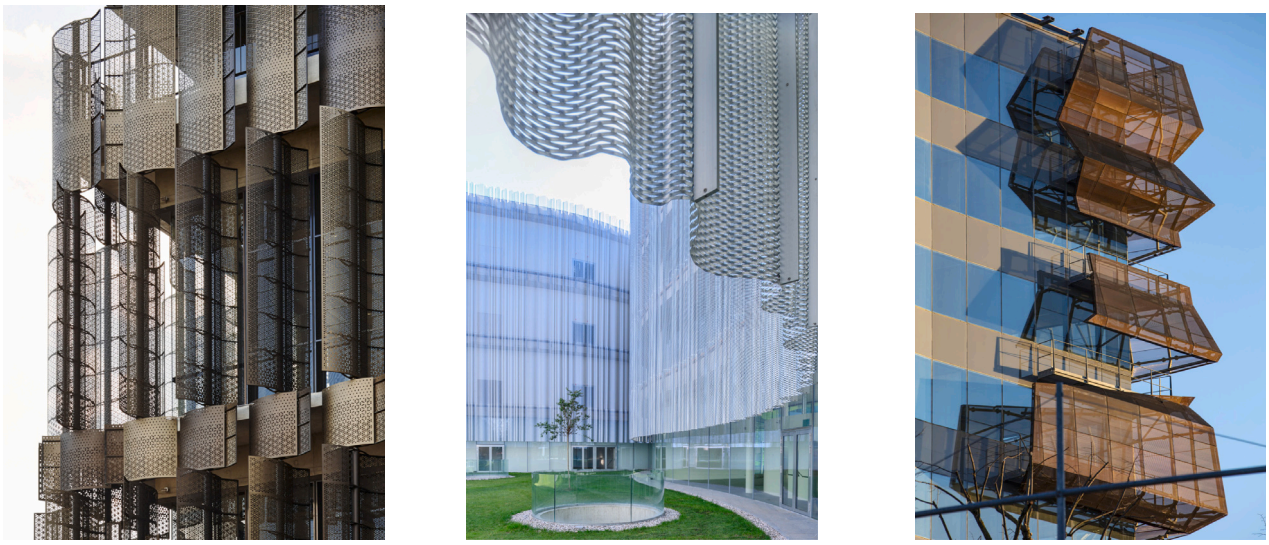

(a) Global Change Institute (Brisbane, Australia). (b) New Bocconi Campus (Milan, Italy). (c) New Eni Headquarters (Milan, Italy).

Fig. 1. Examples of the application of a PDSF system. Close-up on the façade.

Tuned Mass Dampers (TMD) or by altering the object's shape to induce functional aerodynamic effects.

Several authors have suggested that controlling vortex shedding can be achieved by modifying the leading edge of the structure. For instance, in the case of a rectangular cross-section cylinder, adjustments to the corners can promote shear layer reattachment and result in a narrowed wake region (Kwok et al., 1988). Techniques such as slotted and chamfered corners have been shown to effectively reduce cross-wind responses (Sharma et al., 2018; Tamura and Miyagi, 1999).

Another passive solution is based on allowing some of the moving fluid to bleed through the structure into the wake. The key parameter of interest in this case is the porosity (β), defined as the ratio between open surface area and total area. Studies such as Castro (1971) have examined flat plates with different porosity values. They found that for low β values, the wake is dominated by a vortex street, but this effect diminishes as the quantity of bleed air increases. Conversely, high β values suppress vortex shedding, resulting in periodic effects primarily due to far-wake instability. Perforated bluff bodies exhibit similar behavior, with sufficiently high porosity values causing flow through the cavities to resemble a jet-like shape that disrupts the formation of a well-organized Karman vortex street (Teimourian and Teimourian, 2021). An example of these mitigation strategies in action is Rishabh et al. (2019), where wind tunnel tests were conducted on prismatic square buildings with various aerodynamic features such as chamfered corners and single and double vents at different heights.

The primary focus of this research is the application of a porous mesh over a solid structure as a passive wake control method. The flow interaction with a solid structure with a porous covering is complex and depends on multiple parameters, including porosity (β), the distance between the façade and the screen (d), as well as the shape and position of the screen. The literature proposes some studies about the influence of these factors on the response of rectangular cylinders with a unitary aspect ratio. For instance, Gözmen et al. (2013) examined a cylinder with various square permeable façades, manipulating their porosity values and dimensions. They found that higher β values were more effective in suppressing vortex shedding, with an optimal value around $\beta = 0.7$. The ratio between the outer and internal diameter also played a significant role, with peak reduction in turbulent wind observed at values around 0.5 and 1.8. The space between the shroud and the solid structure exhibited some flow recirculation but was insufficient to generate a Karman vortex street (Teimourian and Teimourian, 2021).

Porous screens applied to a building's windward face have shown a decrease in fluctuating pressure and a reduction in dynamic response, particularly within the critical vortex-shedding frequency range (Hu et al., 2017). The central vertical opening appeared to be the most dominant in terms of reducing the response. From a fluid dynamics perspective, the flow through the openings pushes the main shear layer outward upon reaching the leading edge, preventing vortex formation on the side face and leading to reduced fluctuating pressure (Hu et al., 2017). It is important to note that the mesh does not cover the entire structure but only the windward part, demonstrating the effect of partial coverage. Durhasan et al. (2016) investigated a circular cylinder with a perforated fairing mounted downstream ($\beta = 0.6$, arc angle of 180°, $d/D = 0.5$) and reported similar findings. At $Re = 5000$, the shroud elongated the wake region and reduced turbulent shear stresses by approximately 75%, while also decreasing vortex shedding frequency by 50%. Additionally, Belloli et al. (2014) conducted experiments on a scaled model of the top spire of the UniCredit Tower in Milan, where a perforated mesh was tested with positive results.

This research focuses on porosity applications using PDSF on a standard rectangular cylinder. While extensive studies exist for meshed round cylinders, investigations into rectangular cylinders are limited and often performed in rigid models. This research aims to first characterize the VIV on a rectangular cylinder with a $B/D = 3.33$ and then to systematically explore the effect of the PDSF on structural response, thereby contributing to our understanding of the applicability of this technology as a passive mitigation tool against VIV.

2. Setup and methodology

2.1. Semi-aeroelastic model

The model is a 2 m high rectangular cylinder with an aspect ratio of B/D = 3.33, representative of a 100 m high-rise building. The present study is part of a wider ongoing research of building-flow interaction, focused on mean and peak pressure distribution on the façade. Other experimental campaigns have been conducted on the same model (Pomaranzi et al., 2022b; Lamberti et al., 2020; Pomaranzi et al., 2022a) thus its dimensions have not been changed. In the present stage of the research, the authors aim to investigate the structure response when subjected to Vortex-Induced Vibration (VIV). For this purpose, a semi-aeroelastic model is designed: a rigid model of the

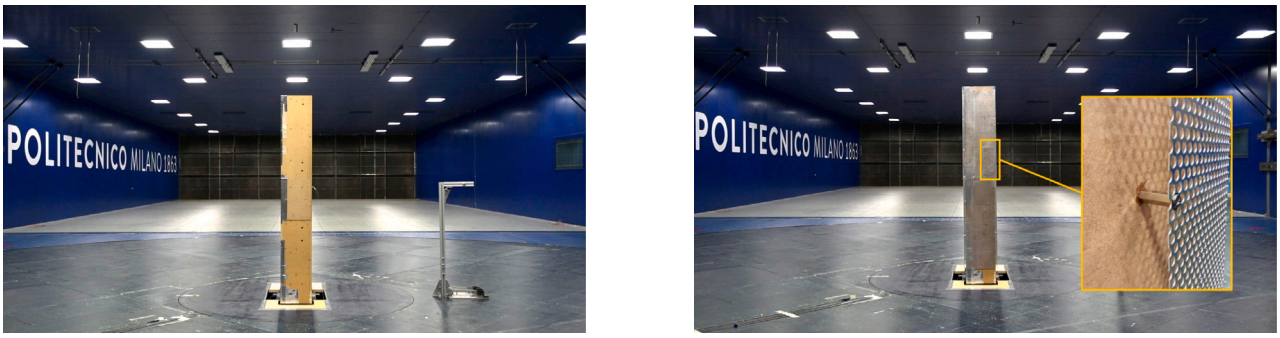

(a) Naked model. (b) PDSF model, zoom on the porous façade.

Fig. 2. Comparison between the front view of the model in the meshed and the naked configuration.

Table 1
From the left: natural frequency in still-air, equivalent modal mass per unit length, adimensional structural damping (cross-wind vibration mode), dimensions of the cross-section, height of the model, Strouhal number and critical free stream velocity without and with PDSF.

Configuration	f_1 [Hz]	m_1 [kg/m]	$\xi_{1,s}$ [%]	B [m]	D [m]	H [m]	St [–]	U_{cr} [m/s]
Naked	1.95	45.2	0.6	1.00	0.30	2.00	0.13	4.4
PDSF	1.88	48.6	0.6	1.04	0.34	2.00	0.15	4.3

building is mounted over an elastic base that allows low-frequency mono-harmonic oscillations in the cross-wind direction.

In the same model, different façade configurations are realized, including the naked configuration, representing single-glazed cladding, and the PDSF configuration, which reproduces a permeable double skin. The latter is achieved by installing a perforated mesh with a porosity $\beta = 55\%$ at a distance $d = 20$ mm from the solid façade. A detail of the PDSF system is reported in Fig. 2b. The employed mesh has a pressure loss coefficient $k = 1.8$, as reported in Pomaranzi et al. (2022b). Modal mass, natural frequency, and damping ratio for the first mode are computed through free motion tests for both configurations. Table 1 summarizes the results. It is worth noting that the installation of the porous screen does not significantly affect the mechanical properties of the oscillating system. In the PDSF model, the first natural frequency is slightly smaller than that of the naked configuration, which is consistent with a 7% increase in modal mass (attributable to the weight of the perforated metal). Additionally, the application of the shroud in the PDSF configuration increases the cross-sectional dimensions, impacting the aspect ratio (see Fig. 4). For both façade configurations (Naked and PDSF), different tests are performed by varying the Scruton coefficient (Sc). Specifically, Sc is adjusted by varying the non-dimensional damping coefficient (ξ_1) using a set of external parasite current dampers. Table 2 provides details of the tested mass-damping configurations. The difference in mass between the naked and PDSF configurations reflects the 9% difference in the value of Sc, with the same damping ratio.

2.2. Tests configurations

All tests are conducted in the atmospheric boundary layer section of Politecnico di Milano wind tunnel (GVPM). The test section measures 14 meters in width, 4 meters in height, and 35 meters in length. Given the objective of investigating Vortex-Induced Vibration (VIV), tests are performed in smooth-flow (with turbulence intensity $I_u < 2.0$ %). The model is allowed to oscillate freely in the cross-wind direction, with the incoming wind perpendicular to the short edge D, as illustrated in Fig. 4. The wind direction is orthogonal to the short edge D. The incoming wind velocity U is measured using a Pitot tube located 1 meter above the ground, positioned 7 meters upwind of the model.

The model is equipped with instruments to measure both accelerations and the external pressure distribution. Four mono-axial accelerometers, PCB model 333b30, are installed at different heights: two

Table 2
Adimensional damping, Scruton number (cross-wind vibration mode) for the different tested configurations.

ξ_1 [%]	Naked $Scruton$ [–]	PDSF $Scruton$ [–]
0.6	4.6	4.2
1.0	–	7.0
1.3	10.0	9.1
2.1	16.2	14.1
3.0	23.1	–

'top accelerometers' at a height (h) of 2 m and two 'middle accelerometers' at a height of 0.6 m above the ground. Additionally, 226 pressure taps are distributed on the model's surface along its height at 8 different levels to capture the temporal and spatial variations of the pressure field on the internal façade (see sketch in Fig. 3). These pressure taps are connected to 8 PSI ESP-32 HD high-speed pressure scanners through rubber tubes with an inner diameter of 1.3 mm. The scanners are connected to an acquisition system with a sampling frequency of 500 Hz. This allows us to fully synchronize pressure data with the building's motion, facilitating the monitoring of pressure variations during both the oscillation build-up and the steady oscillation phases.

Tests are conducted in a progressive regime (PR), involving a continuous increment of wind speed by approximately 0.1 m/s without interrupting the model's motion, and in a transient build-up (BU) mode, starting from a rest position with an initial wind speed of zero. The BU set of measures can be used to understand the onset of the VIV phenomenon. Both PR and BU tests are carried out for various values of Sc and for both façade configurations. Fig. 2 presents the model, with the naked and PDSF configurations, in the wind tunnel test section.

2.3. Data post-processing

Raw pressure data have been post-processed by dividing the signal by the tubing frequency response function to account for the distortions introduced by the measurement system and then filtered at 10 Hz. This is performed to remove high-frequency content and focus on Vortex-Induced Vibration (VIV).

The cross-wind force F_x is computed by performing a spatial integration of the pressure field over the model's surface. This force corresponds to the lift force when the angle of attack is equal to zero, as is the case in the present configuration. Signals from the accelerometers

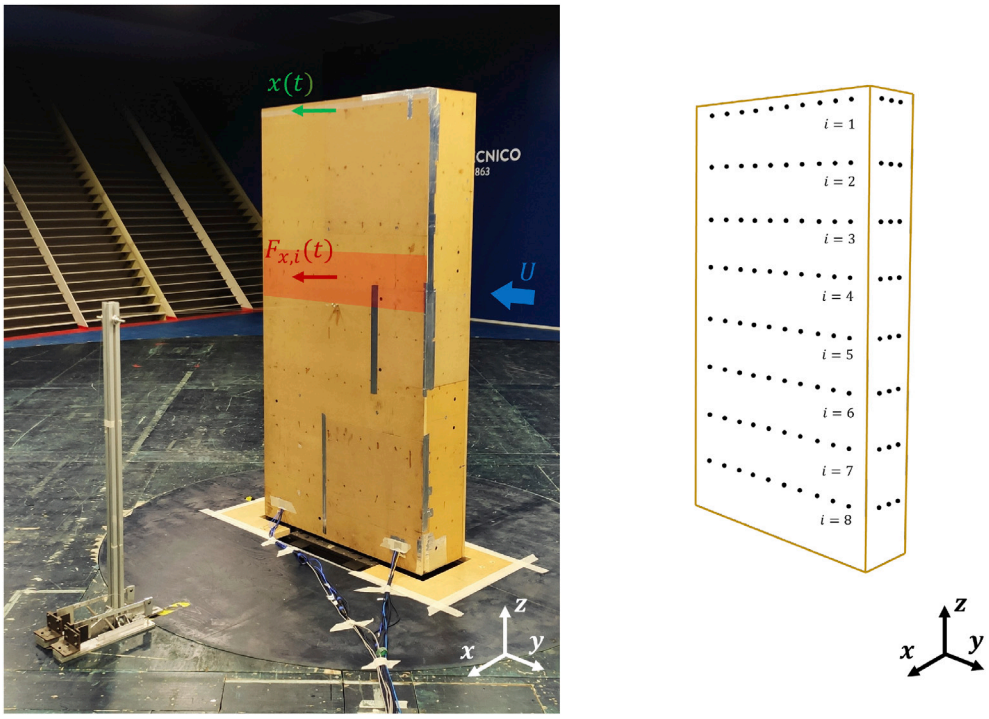

Fig. 3. Left: tested model. The blue arrow indicates the wind direction, the red one the instantaneous cross-wind force amplitude $F_{x,i}(t)$ measured at the ith floor, and in green the top displacement $x(t)$. Right: sketch of the pressure taps distribution on the façade.

(a) Naked model, $B/D = 3.33$. (b) PDSF model, $B/D = 3.06$.

Fig. 4. Quoted sketch of the top view of the model. The blue arrow indicates the wind direction.

have been processed in the frequency domain. Since the structure is interested by mono-harmonic oscillations, the displacement is obtained by dividing the amplitude of acceleration by ω_1^2 and shifting its phase by $\pi\, rad$.

To further characterize the phenomenon, the magnitude-squared coherence (MSC) between the forces along the height and the displacement has been calculated. It is known that when VIV is developed, vortex shedding is characterized by highly space-coherent structures at the oscillating frequency. Thus we choose MSC as a parameter representative of VIV development. MSC between the force coefficient at level 5 (floor located at mid-height) and the other levels (i = $1, 2, 3, \ldots, 8$) is an indicator of vortex shedding spatial coherence. Level 5 is the reference since its position should be less influenced by end-effects. A value of MSC close to the unity at a given frequency indicates that floor i is characterized by the same periodic forcing as floor 5. It is expected that, when VIV is fully developed, MSC will be equal to 1 for all the floors, indicating spatially coherent vortex shedding along the height at the frequency of oscillation. On the other hand, when the structure is not experiencing high-amplitude oscillations either because it is outside the lock-in range or due to the effect of the porous screen, the MSC between different levels is poor.

3. Results

In the following sections, results are first presented for the Naked and then for the PDSF configuration. The focus is on the lock-in region, where the main component of the force spectrum is synchronized with the oscillation.

3.1. Characterization of VIV for the Naked configuration

Fig. 5a presents the polar plot of the normalized amplitude of the first harmonic displacement (x_1/D, blue line, reference on the left axis) and the synchronized component of the total force coefficient ($C_{F_x,1}$, red line, reference on the right axis) for the Naked configuration with $Sc = 4.6$. This case has been chosen as the reference to describe the VIV phenomenon during lock-in. Displacement and force follow the expected amplitude and relative phase trends (Cui et al., 2015; Álvarez et al., 2019).

Results obtained from different initial conditions are reported: specifically, dot markers are representative of the progressive regime (PM) results while the star markers are for the transient build-up (BU) conditions. A good agreement between forces and displacements at PM and BU is found, indicating that VIV develops with the same amplitude independently of the initial wind speed and displacement.

Fig. 6 presents the power spectral densities for different reduced velocities. Blue curves are the PSD of the displacement and red curves are for the cross-wind force. At $U_n = 0.74$ and $U_n = 1.27$, some vortex shedding occurs at $f_n = 1$, but the most energetic component of C_{F_x} shifts to the Strouhal frequency. At the critical speed ($U_n = 1$), both PSDs show a clear peak at $f_n = 1$. Moreover, the energy content is drastically increased compared to the other reduced velocities.

By increasing the Scruton number to $Sc = 10$ (Fig. 5b), the general observations on the phenomenon remain consistent. The characteristic bell-shaped plot of the response is 'smaller' since VIV is triggered at

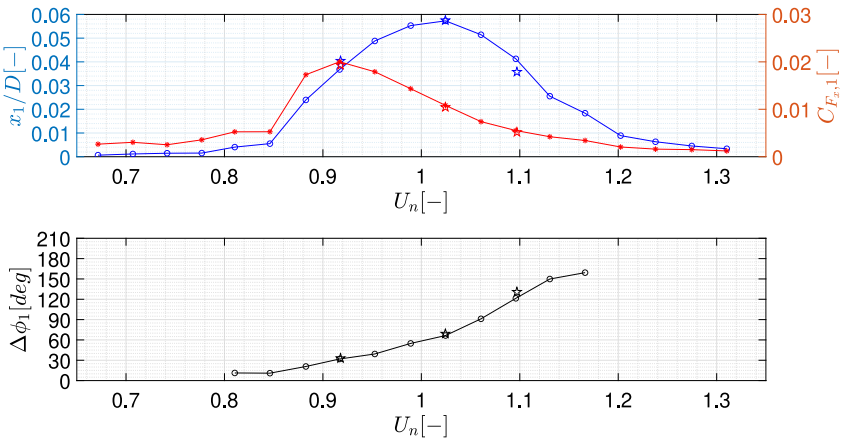

(a) Naked at $Sc = 4.6$.

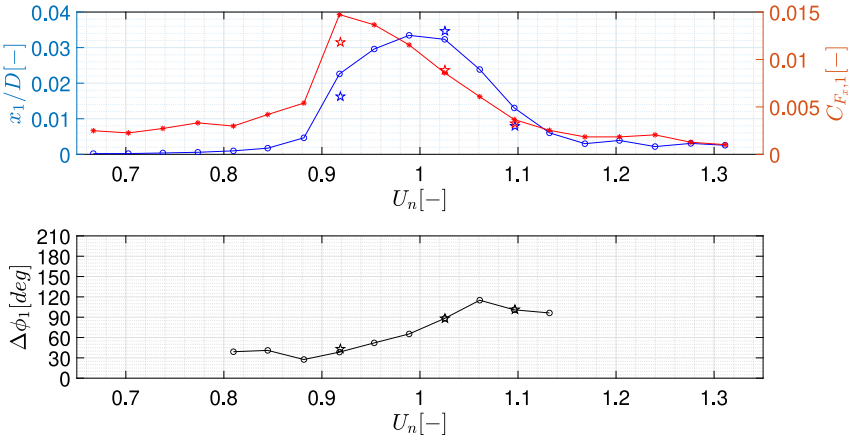

(b) Naked at $Sc = 10.0$.

Fig. 5. Bell-shaped curves of the amplitude of the first harmonic of non-dimensional top displacement (blue) and force coefficient (red). Bottom: phase shift of force relative to the displacement versus reduced velocity (black). The points marked with a star are obtained from build-up tests.

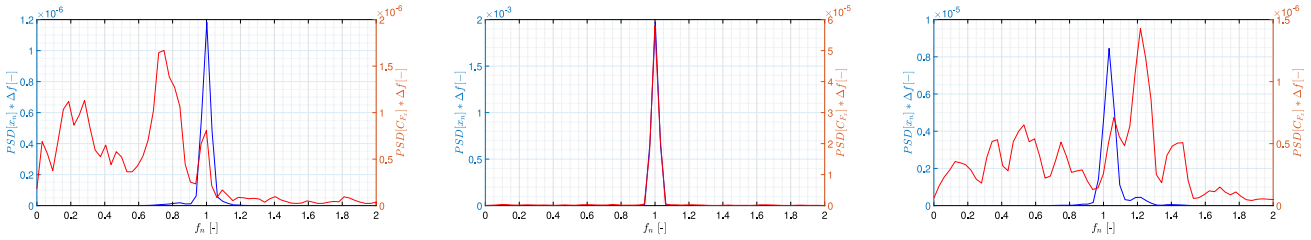

(a) $U_n = 0.74$ (b) $U_n = 1.02$ (c) $U_n = 1.27$

Fig. 6. Normalized power spectral density functions of the top displacement (blue) and cross-wind force (red). Configuration Naked $Sc = 4.6$.

a higher reduced speed ($U_n = 0.89$) and stops earlier, at $U_n = 1.12$, reducing the extension of the lock-in range by approximately 34%. Moreover, the peak amplitude is lower in magnitude, almost half of that in the $Sc = 4.6$ case. The $(C_{F_x,1} - U_n)$ plot follows the same trend. These results are consistent with the literature about VIV on rectangular cylinders (Marra et al., 2015; Tang et al., 2024).

Further increasing the mass-damping coefficient results in no VIV being observed, as no significant force component synchronizes with the displacement: the bells at $Sc = 16.2$ and $Sc = 23.1$ are flat. Compared with the literature results, VIV in the present case is suppressed at a lower Scruton value than the ones proposed by Marra et al. (2015), Tang et al. (2024). This discrepancy may be reconducted to the different setup used for the tests: the present model mimics a building (ground-clamped at the base), while Marra et al. (2015) and Tang et al. (2024) tested a suspended prism.

To understand the physical reason behind synchronization, it is necessary to examine local forces, as will be analyzed in the following paragraphs.

3.1.1. Coherence analysis, Low Scruton configuration

The first case here analyzed is the Naked structure at the lowest Scruton coefficient ($Sc = 4.6$). A few representative points of the

bell-shaped response have been selected to describe the evolution of VIV.

In Fig. 7a, the time history of the structural top displacement (right axis) and the force coefficients obtained by integrating the pressure signals on the central floors number 4 and 5 (left axis) are plotted for the following cases.

- $U_n = 0.74$: At this point, which falls outside the synchronization range, the system exhibits small amplitude oscillations. The force has a very low power content at $f_n = 1$, and the most energetic harmonics are around $f_n = 0.74$. The synchronous force signals are out of phase with respect to the displacement, and this is evident along the height, as indicated by the magnitude squared coherence plots (Fig. 7b). At $f_n = 1$, forces and oscillation show a maximum coherence value of 0.5, while at $f_n = 0.74$, where the primary vortex shedding phenomenon occurs, peaks of 0.9 are reached.
- $U_n = 0.84$: This marks the lower limit of the synchronization range. The main frequency of vortex shedding is now $f_n = 1$, and the harmonic at $f_n = 0.84$ becomes secondary (Fig. 8a). The displacement signal exhibits regular behavior in the time domain, characterized by constant oscillations, and its amplitude increases compared to the point at $U_n = 0.81$ as the magnitude squared coherence (MSC) between $C_{F_x,i}$ and x approaches 0.9 (Fig. 8b). The force signals are more coherent with the reference level at $f_n = 1$, indicating the presence of a correlated phenomenon along the height at the oscillation frequency. Some degree of coherence between floors is also present at low reduced frequencies, around $f_n = 0.2$, but it is associated with low energy content in the power spectral density (PSD), so it can be regarded as secondary.
- $U_n > 0.84$ (Lock-In Region): In this range, the system is in a lock-in condition: the signals are synchronized, and the vortex shedding frequency equals the structure's oscillation frequency (Fig. 9a). At $f_n = 1$, the value of MSC is 1, indicating a perfect correlation between the displacement and the forces, as well as between the forces along the height (Fig. 9b). The maximum reduced displacement amplitude of $x_n = 0.5$ is reached at $U_n = 1.02$.
- $U_n > 1.20$ (Outside Lock-In Region): At higher wind speeds, outside the lock-in region, the displacement signal displays irregular behavior in the time domain, alternating between high-amplitude and low-amplitude cycles. In the PSD of the force coefficients, some harmonics in the proximity of the oscillation frequency are still present, but the highest energy content shifts to $f_n = U_n$, following the Strouhal law. The coherence between $C_{F_x,i}$ and x almost drops to zero at $f_n = 1$, while some degree of correlation is present at $f_n = 1.27$, but the MSC value is not constant among the planes.

From the analysis of the reference Naked-$Sc = 4.6$ case, it results that high-amplitude oscillations at lock-in are always characterized by high coherence between the pressure integrals along the height. VIV is known to be highly state-dependent: when the system oscillates with certain amplitudes, spatial correlation is naturally triggered by the movement, leading to coherent vortex shedding (VS) that feeds the vibrations. Therefore, the coherence between the structural response and the forcing signals increases as the oscillation amplitude rises, reaching its maximum during the peak of VIV. When the correlation decreases, regular oscillation can still occur, but its amplitude is much lower and not stable over time (see Fig. 10).

3.1.2. Coherence analysis, Mid-Scruton configuration

From a phenomenological point of view, the behavior of the oscillating structure at $Sc = 10$ is similar to that of the low-Sc case.

The range of wind speeds at which the lock-in condition is verified is shorter, as expected since the dissipation capabilities of the system are higher (as already highlighted in Fig. 5b). The maximum VIV condition still occurs at $U_n = 1$ and is characterized by coherence functions close to unity for all floors (Fig. 11).

3.1.3. Coherence analysis, High Scruton configuration

When the Sc number is increased beyond $Sc = 16.2$ (Figs. 12 and 13), the system no longer exhibits high-amplitude oscillations, even when considering the critical velocity. Both cases exhibit a displacement time history characterized by 'pulsating' behavior, with no stable amplitude of oscillation. The force coefficients $C_{Fx,i}$ have their main energetic content at $f_n = 1$ (*i.e.* the lock-in region), indicating some synchronized phenomenon. However, the MSC with the structural response is very low, below 0.6 (Fig. 12b).

At $Sc = 23.1$, no lock-in is observed, and no significant VIV is measured, even at $U_n = 1.02$. The PSDs of the signals are not monoharmonic (Fig. 13a), and the coherence functions are consistently below 0.6 across the spectrum (Fig. 13b), indicating uncorrelated force signals with the displacement along the height.

At higher values of mass damping, it is no longer possible to observe vortex-induced vibrations. For this reason, the parametric study on the Scruton number ends with $Sc = 23.1$. It can be concluded that the effect of the mass-damping coefficient is to reduce the amplitude of VIV at all wind velocities. Some lock-in is still present at the critical speed, but the signals are no longer coherent.

3.2. Characterization of VIV for the PDSF configuration

After the installation of the porous mesh, the tests are repeated under the same conditions. The first configuration analyzed has $\xi_1 = 0.6\%$. Considering the definition of the Scruton number, when mass-damping is normalized by the increased cross-section dimensions of the shroud, a lower coefficient is obtained compared to the naked case with the same damping (see Table 1).

As for the PDSF case, the polar plot of the normalized displacements (blue curve) and cross-wind force (red curve) is presented in Fig. 14. Dot markers are referred to as the PR conditions, while the star markers are referred to as the BU.

For the lowest Sc (Fig. 14a), the PDSF model exhibits the same force and displacement trends as the naked counterpart, both in terms of amplitude and phase. The PDSF tests in lock-in conditions allow for the computation of the Strouhal number considering the mean wind speed and the oscillation frequency of the model, as proposed by Choi and Kwon (2000). It results that the Strouhal number of the PDSF configuration is smaller than the Naked one; this is compatible with an increased cross-section dimension of the prism ($B/D = 3.06$) with respect to the naked case ($B/D = 3.33$). This finding may suggest that the model in the low-Sc PDSF configuration could behave like a solid one with increased cross-section dimensions, at least with regard to the Strouhal number.

As Sc increases, the PDSF configuration exhibits a different behavior than the naked configuration. Referring to the structural response and force curves in Figs. 14b and 14c, VIV is not appearing until a threshold velocity is reached ($U_n = 0.95$ at $Sc = 7.0$, $U_n = 0.99$ at $Sc = 9.1$). At the critical speed, both quantities are in quadrature and reach their peak values, indicating the full development of VIV.

Once the phenomenon is triggered, it evolves and ceases similarly to the naked case. In the desynchronization range, the structure oscillates with amplitudes comparable to its solid counterpart, driven by a synchronous force shifted by 120°. Focusing on the right branch of the normalized displacement bell, the PDSF configuration behaves as the Naked one. However, unlike the solid structure, the synchronization of $C_{F_x,1}$ and x_1/D is sudden, and their peaks occur simultaneously. For such configurations, it is also to highlight a dependency on the initial conditions: star markers in Figs. 14b and 14c are showing no VIV for the system. Hence, if critical speed is reached in BU conditions, no relevant force or displacement is measured at $f_n = 1$.

In contrast, when the structure is already vibrating on its own (PR — dot markers in the plots), high-amplitude oscillations are induced at the critical wind velocity.

As in the Naked case, further insights into the mechanism governing synchronization during lock-in can be gained from the study of pressure integrals along the height.

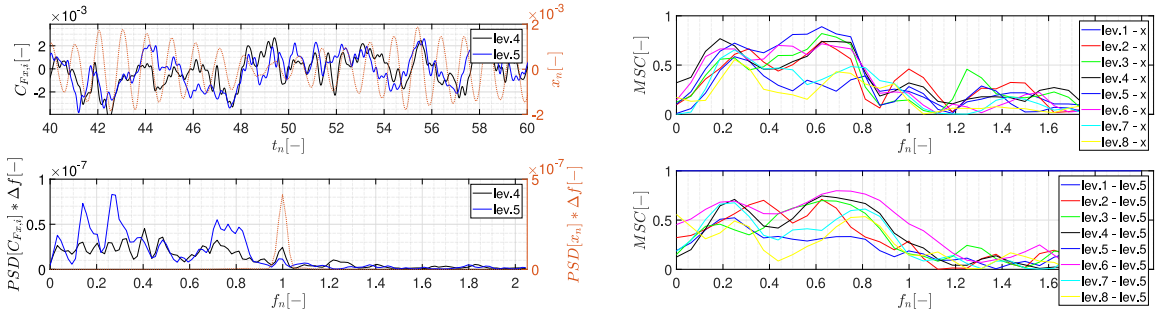

(a) Zoomed time history (up), Power spectral density (down). Normalized displacement (right axis, orange curve) and force coefficient at levels 4 and 5 (left axis).

(b) Magnitude Squared Coherence between force coefficient at level i and displacement (up), between force coefficient at level i and level 5 (down).

Fig. 7. Configuration Naked, $Sc = 4.6$, $U_n = 0.74$.

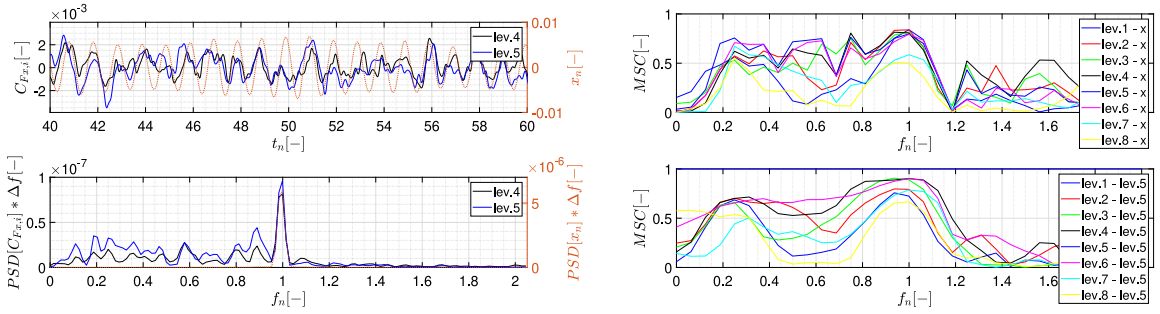

(a) Zoomed time history (up), Power spectral density (down). Normalized displacement (right axis, orange curve) and force coefficient at levels 4 and 5 (left axis).

(b) Magnitude Squared Coherence between force coefficient at level i and displacement (up), between force coefficient at level i and level 5 (down).

Fig. 8. Configuration Naked, $Sc = 4.6$, $U_n = 0.84$.

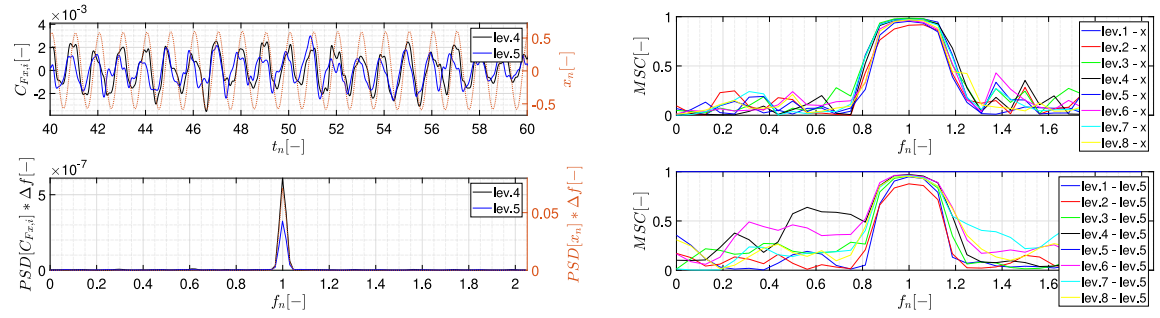

(a) Zoomed time history (up), Power spectral density (down). Normalized displacement (right axis, orange curve) and force coefficient at levels 4 and 5 (left axis).

(b) Magnitude Squared Coherence between force coefficient at level i and displacement (up), between force coefficient at level i and level 5 (down).

Fig. 9. Configuration Naked, $Sc = 4.6$, $U_n = 1.02$.

3.2.1. *Coherence analysis, Low Scruton configuration*

The first configuration considered is PDSF-$Sc = 4.2$, and the same representative points chosen for Naked-$Sc = 4.6$ are analyzed. This configuration exhibits several similarities with its naked counterpart:

- Prior to entering the lock-in zone, at $U_n = 0.76$, there is no synchronization between the displacement and force signals, and the coherence value at $f_n = 1$ is below 0.5. The power spectral density (PSD) plot in Fig. 15a suggests that most of the energy content of the force is in the lower part of the spectrum at $f_n = 0.25$, in contrast to the naked case, where the main frequency of vortex shedding is at $f_n = U_n$. It is worth noting that the mean square coherence (MSC) for $f_n < 1$ among the forces along the height shows values above 0.5. As expected, the floors less correlated with the central one are the ones at the top (floors 1 and 2) and the one at the bottom (floor 8) (Fig. 15b).

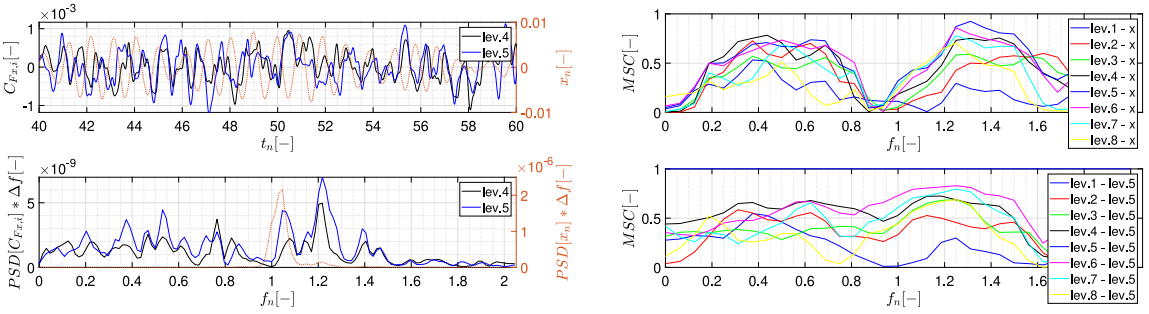

(a) Zoomed time history (up), Power spectral density (down). Normalized displacement (right axis, orange curve) and force coefficient at levels 4 and 5 (left axis).

(b) Magnitude Squared Coherence between force coefficient at level i and displacement (up), between force coefficient at level i and level 5 (down).

Fig. 10. Configuration Naked, $Sc = 4.6$, $U_n = 1.27$.

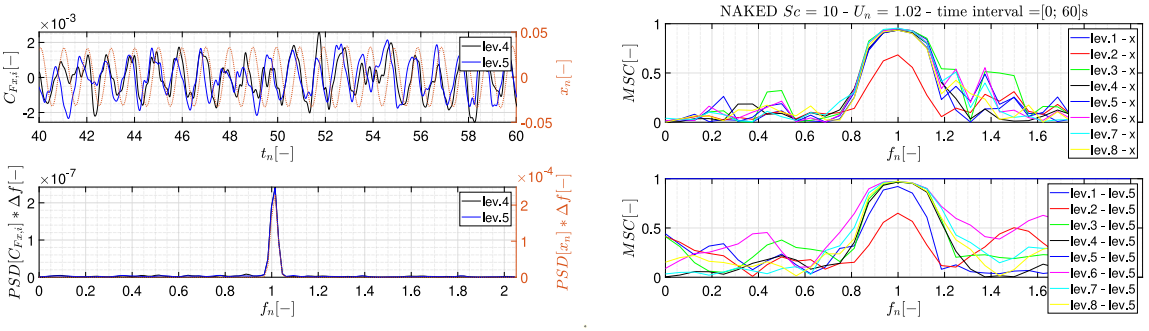

(a) Zoomed time history (up), Power spectral density (down). Normalized displacement (right axis, orange curve) and force coefficient at levels 4 and 5 (left axis).

(b) Magnitude Squared Coherence between force coefficient at level i and displacement (up), between force coefficient at level i and level 5 (down).

Fig. 11. Configuration Naked, $Sc = 10$, $U_n = 1.02$.

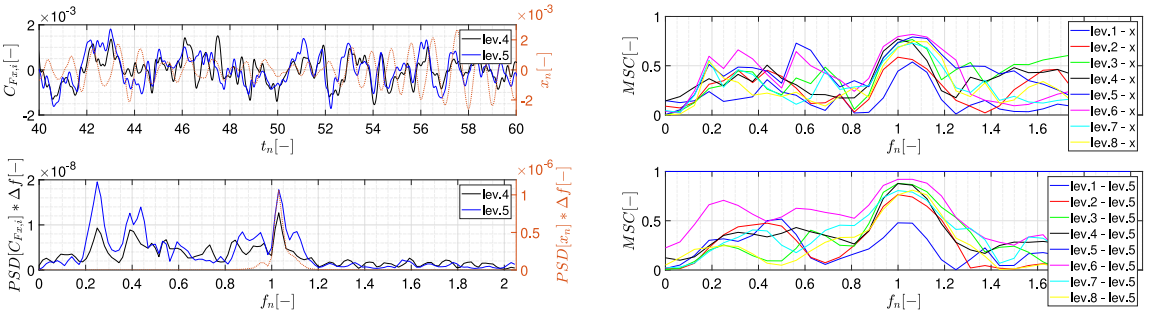

(a) Zoomed time history (up), Power spectral density (down). Normalized displacement (right axis, orange curve) and force coefficient at levels 4 and 5 (left axis).

(b) Magnitude Squared Coherence between force coefficient at level i and displacement (up), between force coefficient at level i and level 5 (down).

Fig. 12. Configuration Naked, $Sc = 16.2$, $U_n = 1.02$.

- At $U_n = 0.83$, perfect synchronization between displacement and force coefficients is observed (Fig. 16a). The MSC values indicate coherence close to unity at $f_n = 1$ and above 0.5 in the lower part of the spectrum (Fig. 16b). From this point, with an increase in wind speed, the PSD functions remain perfectly monoharmonic at $f = f_1$, and both the MSC functions approach 1 at the same frequency. The amplitude of oscillation increases monotonically and reaches a maximum at $U_n = 0.98$ (Fig. 17a). The peak standard deviation is 22% higher compared to the naked case in the same configuration.
- Outside of the lock-in range of velocities, the point at $U_n = 1.27$ shows that, similar to the naked reference case, the displacement exhibits a 'pulsating' low-amplitude behavior in the time domain. Despite this, the PSD function of force coefficients still contains some harmonic components at $f = f_1$ (Fig. 18a). As in the naked case, the MSC functions do not peak at $f_n = 1$, but the force

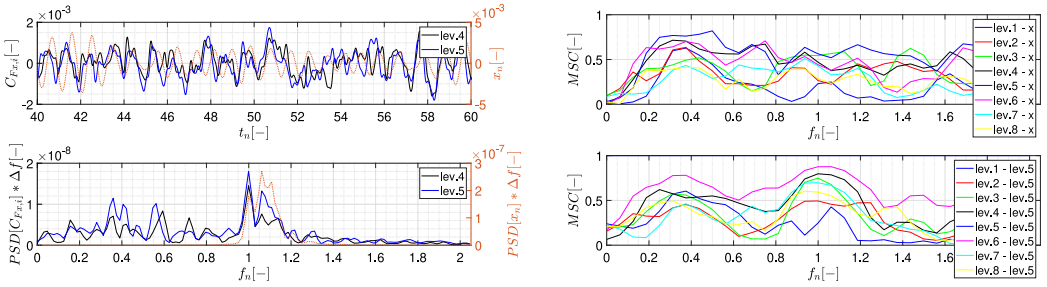

(a) Zoomed time history (up), Power spectral density (down). Normalized displacement (right axis, orange curve) and force coefficient at levels 4 and 5 (left axis).

(b) Magnitude Squared Coherence between force coefficient at level i and displacement (up), between force coefficient at level i and level 5 (down).

Fig. 13. Configuration Naked, $Sc = 23.1$, $U_n = 1.02$.

coefficients appear generally more correlated along the height, mainly at low frequencies (Fig. 18b).

3.2.2. Coherence analysis, Mid Scruton configuration

When the Scruton number is increased, the system changes behavior. In the case of Scruton number $Sc = 7.0$, we observed varying structural responses at $U_n = 0.98$, depending on how the critical vortex shedding velocity is reached:

- When the wind speed is increased step by step, (progressive regime — PR, Fig. 19), the system exhibits high-amplitude VIV, similarly to the Naked counterpart. Analysis of the PSD reveals perfect synchronization between displacement and forces at $f_n = 1$, and the MSC functions approach unity. VIV and lock-in occur as the wind speed reaches the critical vortex shedding velocity. Despite the double skin, this phenomenon shares characteristic features with a solid structure.
- When the critical speed is reached starting from a still model in still air (build-up — BU, Fig. 20), the system does not show any significant oscillation, synchronization is absent, and force and displacement signals appear uncorrelated. The PSD and MSC functions resemble those obtained at lower reduced speeds, and the highly correlated phenomenon in the lower part of the spectrum persists. Specifically, the PSD in Fig. 20a shows the most energetic harmonics in the lowest part of the spectrum, at $f_n = [0.2–0.4]$. The coherence functions (Fig. 20b) show high values of MSC between forces and displacement, but along the height, only the floors closer to the reference floor share values of MSC above 0.8. This low-frequency, highly coherent phenomenon is characteristic of the PDSF configuration and appears whenever the system is not in a lock-in condition. It could be related to air circulation in the gap between the two façade layers. However, this phenomenon does not seem to be related to VIV, as it occurs with the same intensity at all tested wind velocities.
- In a third test, starting from BU conditions, the quiet system was perturbed by external input (EI, Fig. 21). This was sufficient to trigger VIV. The externally-excited system exhibited VIV similar to the progressive regime case. The magnitude of the external input is challenging to quantify, but qualitatively, it triggered the correlation of forces along the height.

The case PDSF-$Sc = 9.1$ shares the same features as the one just described, thus results have not been reported for brevity. As already shown for the $Sc = 7.0$, when $Sc = 9.1$ high-amplitude VIV is unlikely to occur from the rest position for the PDSF configuration. Porosity prevents the onset of spatially coherent vortex shedding. However, in the most critical condition (at $U_n = 1$), a correlation could randomly occur if the system is somehow perturbed, as observed in the EI case with $Sc = 0.7$.

To investigate the building behavior at higher Scruton, tests have been carried out considering the PDSF-$Sc = 14.1$ configuration. For this case, no relevant oscillation has been measured in any scenario: the mass-damping coefficient is high enough to suppress any vortex-induced vibration. Results from this case are omitted since they do not add any significant element to the analysis.

4. Conclusions

The present study has addressed the issue of vortex-induced vibrations in a rectangular cylinder with an aspect ratio of $B/D = 3.33$. The primary objective was to investigate the impact of a permeable double-skin façade (PDSF) by comparing the structural response of the building, both with and without the porous layer.

The analysis of VIV was conducted considering its dependence on the Scruton number. To understand the overall behavior of the oscillating structure, the coherence function between the pressure integral on the floors and the structural response has been considered. The results obtained from the single-façade model are used as a reference for a comparative study with the PDSF configuration. Key findings for the naked configuration can be summarized as follows:

- Within the entire lock-in region, the MSC between the lift components along the height of the model and the displacement approaches unity, as well as the MSC between forces of the individual floors.
- At higher reduced velocities, within the desynchronization range, forces, and motion become less coherent. In particular, the top floors experience a more consistent drop in MSC at the Strouhal frequency due to the interference of end effects on vortex shedding.
- The lock-in region is characterized by significant synchronized oscillations for $Sc < 16.2$. Increasing mass-damping results in lower energy content associated with the frequency of motion and reduced coherence along the building's height.

Turning to the results for the PDSF façade configuration, the main findings can be summarized as follows:

- At the lowest mass-damping configuration ($Sc = 4.2$), the behavior of the PDSF structure aligns with that of a solid cylinder with an increased aspect ratio, considering the outer dimension of the double skin (as it was solid). Additionally, the pressure integral and structural response coherence are comparable to the naked configuration. Moreover, the experimentally computed Strouhal number matches the one suggested in the literature for a solid rectangular cylinder with an aspect ratio of $B/D = 3.06$. These

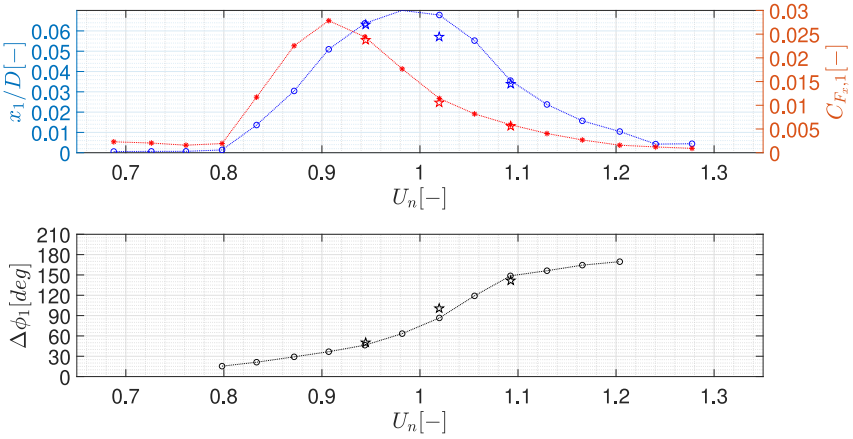

(a) PDSF $Sc = 4.2$.

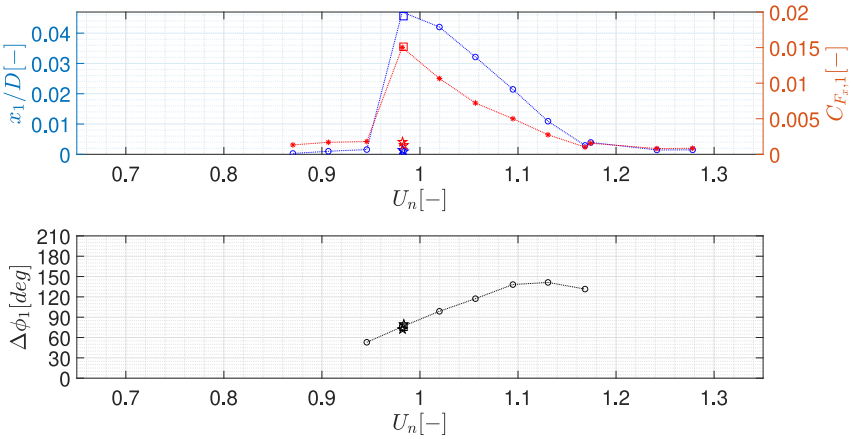

(b) PDSF $Sc = 7.0$.

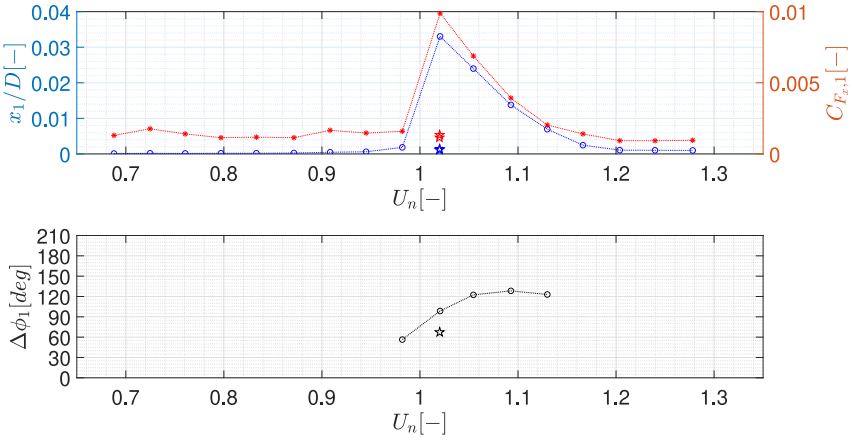

(c) PDSF $Sc = 9.1$.

Fig. 14. Top: bell-shaped curves of the amplitude of the first harmonic of adimensional top displacement (blue) and force coefficient (red). Bottom: phase of force relative to the displacement versus reduced velocity (black). The points marked with a star are obtained from build-up tests.

findings support the idea that the low-Sc PDSF structure behaves like a low-Sc fully solid structure with an enhanced cross-section.

- As the Scruton number increases ($7 < Sc < 9$), the behavior of the PDSF diverges from that of the naked configuration. For $U_n < 0.95$, the porous screen effectively inhibits oscillations, and the forces along the height are not coherent at the frequency of motion. At the critical vortex-shedding speed, the system's response exhibits dependency on initial conditions: in the build-up condition (BU), no significant system response is observed in the predicted lock-in condition, with very low force coherence along the height. Conversely, the progressive regime (PR) or external excitation (EI) triggers VIV with characteristics similar to the naked counterpart (*i.e.*, synchronized and high correlation between displacement and force signals).

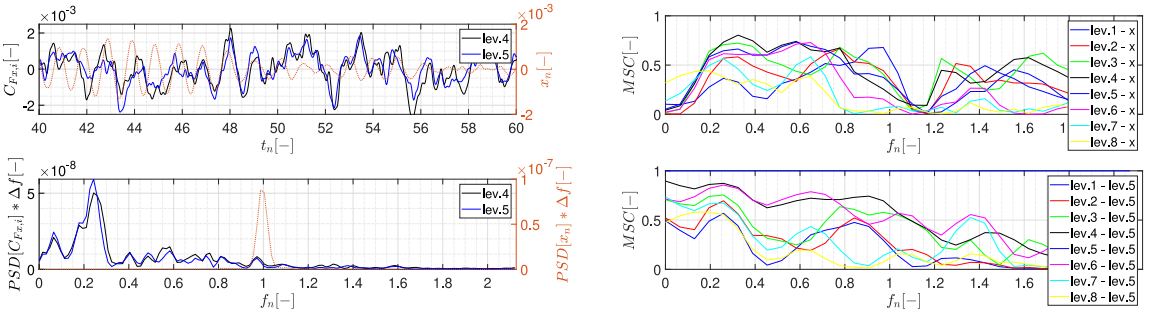

(a) Zoomed time history (up), Power spectral density (down). Normalized displacement (right axis, orange curve) and force coefficient at levels 4 and 5 (left axis).

(b) Magnitude Squared Coherence between force coefficient at level i and displacement (up), between force coefficient at level i and level 5 (down).

Fig. 15. Configuration PDSF, $Sc = 4.2$, $U_n = 0.76$.

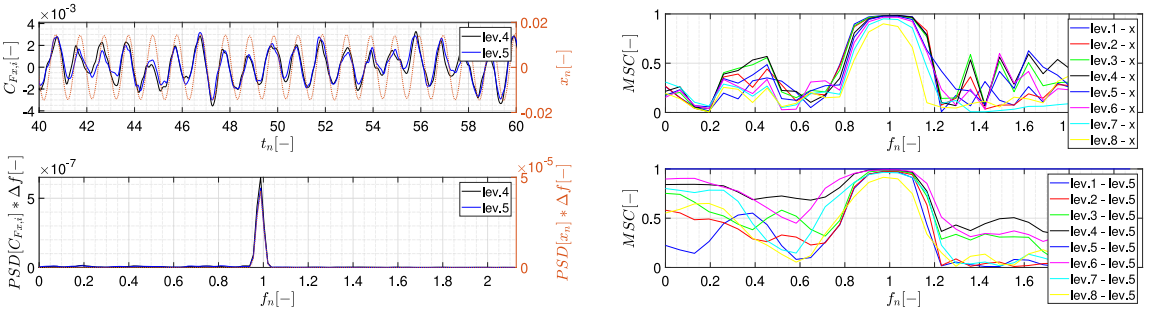

(a) Zoomed time history (up), Power spectral density (down). Normalized displacement (right axis, orange curve) and force coefficient at levels 4 and 5 (left axis).

(b) Magnitude Squared Coherence between force coefficient at level i and displacement (up), between force coefficient at level i and level 5 (down).

Fig. 16. Configuration PDSF, $Sc = 4.2$, $U_n = 0.83$.

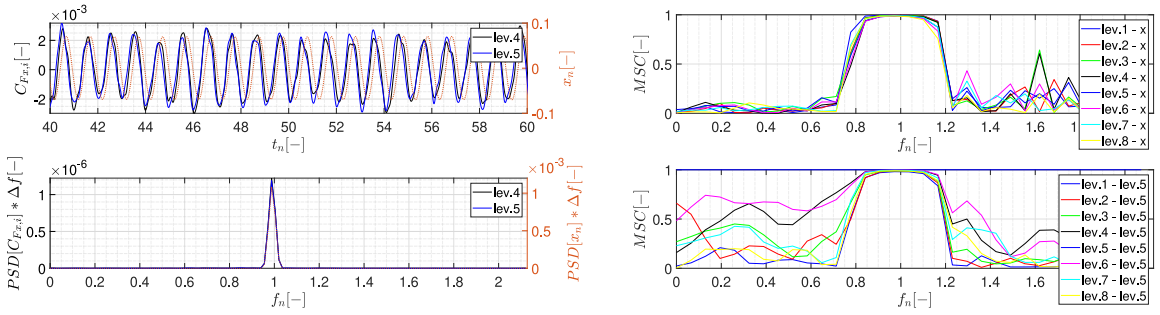

(a) Zoomed time history (up), Power spectral density (down). Normalized displacement (right axis, orange curve) and force coefficient at levels 4 and 5 (left axis).

(b) Magnitude Squared Coherence between force coefficient at level i and displacement (up), between force coefficient at level i and level 5 (down).

Fig. 17. Configuration PDSF, $Sc = 4.2$, $U_n = 0.98$.

- A noteworthy difference between the PDSF and the naked case is the presence of sub-harmonics in the power spectral density (PSD) of the force at 0.2–0.4 reduced frequency. In the same frequency range, forces exhibit a high correlation along the height, suggesting a low time-scale phenomenon independent from VIV that could be related to the gap flow developed between the two layers of the façade. Further research is needed to understand its nature and connection with the installed porous medium.

It has been shown that the implementation of a double-skin porous façade significantly impacts the onset of the VIV phenomenon. While the mass-damping characteristics of the oscillating structure still play a role, promising results in terms of oscillation attenuation can be

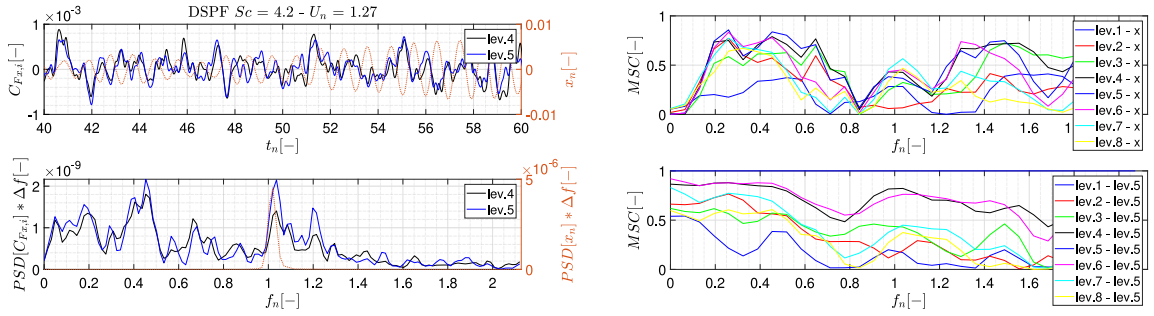

(a) Zoomed time history (up), Power spectral density (down). Normalized displacement (right axis, orange curve) and force coefficient at levels 4 and 5 (left axis).

(b) Magnitude Squared Coherence between force coefficient at level i and displacement (up), between force coefficient at level i and level 5 (down).

Fig. 18. Configuration PDSF, $Sc = 4.2$, $U_n = 1.27$.

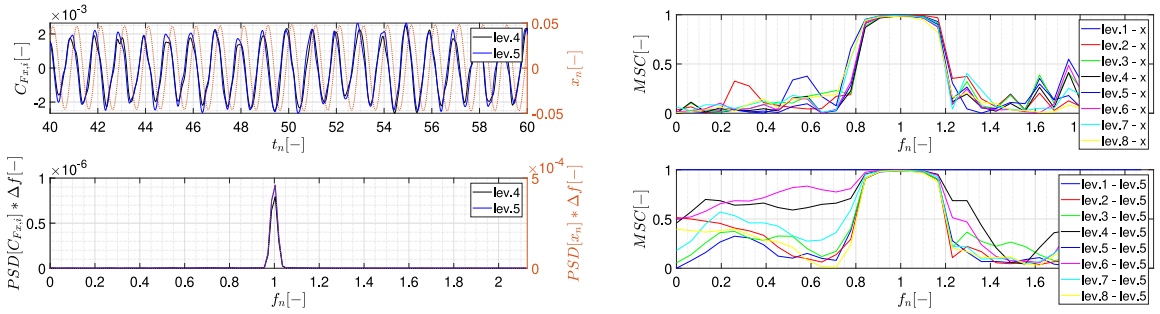

(a) Zoomed time history (up), Power spectral density (down). Normalized displacement (right axis, orange curve) and force coefficient at levels 4 and 5 (left axis).

(b) Magnitude Squared Coherence between force coefficient at level i and displacement (up), between force coefficient at level i and level 5 (down).

Fig. 19. Configuration PDSF, $Sc = 7.0$, $U_n = 0.98$, PROGRESSIVE REGIME.

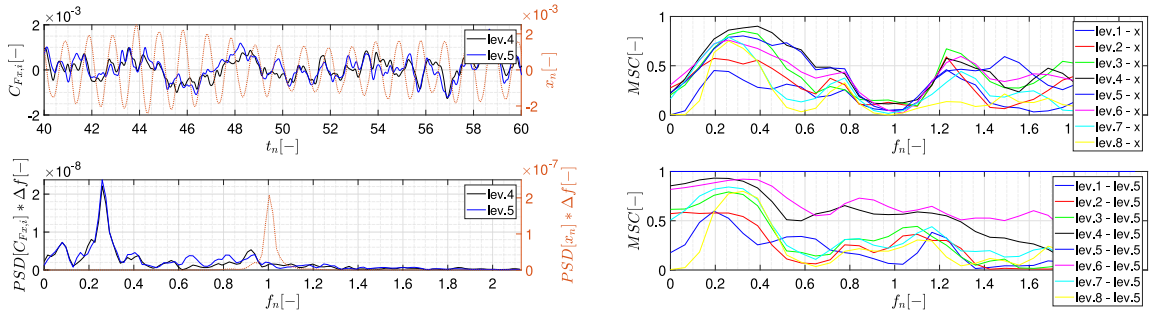

(a) Zoomed time history (up), Power spectral density (down). Normalized displacement (right axis, orange curve) and force coefficient at levels 4 and 5 (left axis).

(b) Magnitude Squared Coherence between force coefficient at level i and displacement (up), between force coefficient at level i and level 5 (down).

Fig. 20. Configuration PDSF, $Sc = 7.0$, $U_n = 0.98$, BUILD UP.

achieved with the PDSF solution. VIV proves to be a state-dependent phenomenon, with its onset strongly affected by the presence of spatially coherent vortexes. In the case of single-façade structures, this condition is consistently met within the lock-in range, independently from the initial state of the system; with the outer porous layer instead, the VIV onset becomes dependent on the initial state. For rest initial condition, the PDSF is able to prevent high-amplitude oscillations due to a reduced correlation between pressure integrals and motion of the structures.

This study has characterized the way the PDSF is able to affect the onset of the VIV in a rectangular cylinder, highlighting the role of spatial correlation. As a consequence, it emerges the possibility of optimizing the placement of porous elements on the façade, particularly focusing on areas where vortex shedding exhibits greater correlation.

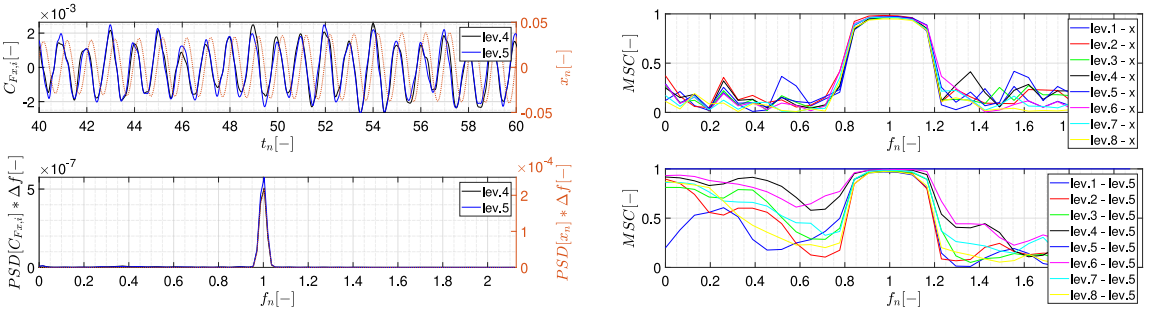

(a) Zoomed time history (up), Power spectral density (down). Normalized displacement (right axis, orange curve) and force coefficient at levels 4 and 5 (left axis).

(b) Magnitude Squared Coherence between force coefficient at level i and displacement (up), between force coefficient at level i and level 5 (down).

Fig. 21. Configuration PDSF, $Sc = 7.0$, $U_n = 0.98$, EXTERNAL INPUT.

Asymmetric distributions over the central floors and at the front-wind edges may represent a viable strategy for achieving an optimized and cost-efficient PDSF solution for VIV suppression.

CRediT authorship contribution statement

Marcello Catania: Conceptualization, Data curation, Formal analysis, Investigation, Methodology, Software, Writing – original draft, Writing – review & editing. **Giulia Pomaranzi:** Conceptualization, Methodology, Supervision, Validation, Writing – original draft, Writing – review & editing. **Alberto Zasso:** Methodology, Supervision, Validation, Writing – review & editing.

Declaration of competing interest

The authors declare that they have no known competing financial interests or personal relationships that could have appeared to influence the work reported in this paper.

Data availability

Data will be made available on request.

References

Álvarez, A., Nieto, F., Nguyen, D., Owen, J., Hernández, S., 2019. 3D LES simulations of a static and vertically free-to-oscillate 4:1 rectangular cylinder: Effects of the grid resolution. J. Wind Eng. Ind. Aerodyn. 192, 31–44. http://dx.doi.org/10.1016/j.jweia.2019.06.012, URL https://www.sciencedirect.com/science/article/pii/S0167610519305203.

Bartoli, G., Righi, M., 2006. Flutter mechanism for rectangular prisms in smooth and turbulent flow. J. Wind Eng. Ind. Aerodyn. 94 (5), 275–291.

Belloli, M., Rosa, L., Zasso, A., 2014. Wind loads and vortex shedding analysis on the effects of the porosity on a high slender tower. J. Wind Eng. Ind. Aerodyn. 126, 75–86.

Castro, I., 1971. Wake characteristics of two-dimensional perforated plates normal to an air-stream. J. Fluid Mech. 46 (3), 599–609.

Choi, C.K., Kwon, D.K., 2000. Determination of the strouhal number based on the aerodynamic behavior of rectangular cylinders. Wind Struct. Int. J. 3 (3), 209–220. http://dx.doi.org/10.12989/was.2000.3.3.209, URL https://www.scopus.com/inward/record.uri?eid=2-s2.0-0034270669&doi=10.12989/2fwas.2000.3.3.209&partnerID=40&md5=a8c0e2ce29ebb34e1b329203c6f75cf3 Cited by: 11.

Corless, R., Parkinson, G., 1988. A model of the combined effects of vortex-induced oscillation and galloping. J. Fluids Struct. 2 (3), 203–220. http://dx.doi.org/10.1016/S0889-9746(88)80008-2, URL https://www.sciencedirect.com/science/article/pii/S0889974688800082.

Cui, Z., Zhao, M., Teng, B., Cheng, L., 2015. Two-dimensional numerical study of vortex-induced vibration and galloping of square and rectangular cylinders in steady flow. Ocean Eng. 106, 189–206. http://dx.doi.org/10.1016/j.oceaneng.2015.07.004, URL https://www.sciencedirect.com/science/article/pii/S002980181500308X.

Darkwa, J., Li, Y., Chow, D., 2014. Heat transfer and air movement behaviour in a double-skin façade. Sustainable Cities Soc. 10, 130–139. http://dx.doi.org/10.1016/j.scs.2013.07.002, URL https://www.sciencedirect.com/science/article/pii/S2210670713000425.

Deniz, S., Staubli, T., 1997. Oscillating rectangular and octagonal profiles: interaction of leading-and trailing-edge vortex formation. J. Fluids Struct. 11 (1), 3–31.

Durhasan, T., Aksoy, M., Pinar, E., Ozkan, G., Akilli, H., Sahin, B., 2016. Vortex street suppression of a circular cylinder using perforated semi-circular fairing in shallow water. Exp. Therm Fluid Sci. 79, 101–110.

Giosan, I., Eng, P., 2013. Vortex shedding induced loads on free standing structures. In: Structural Vortex Shedding Response Estimation Methodology and Finite Element Simulation, vol. 42.

Gözmen, B., Akilli, H., Şahin, B., 2013. Vortex control of cylinder wake by permeable cylinder. J. Fac. Eng. Archit. 28 (2), 77–85.

Haan, Jr., F., Kareem, A., 2009. Anatomy of turbulence effects on the aerodynamics of an oscillating prism. J. Eng. Mech. 135 (9), 987–999.

Hémon, P., Santi, F., 2002. On the aeroelastic behaviour of rectangular cylinders in cross-flow. J. Fluids Struct. 16 (7), 855–889.

Holmes, J., Bekele, S., 2020. Wind Loading of Structures, fourth ed. http://dx.doi.org/10.1201/9780429296123.

Hu, G., Hassanli, S., Kwok, K., Tse, K., 2017. Wind-induced responses of a tall building with a double-skin façade system. J. Wind Eng. Ind. Aerodyn. 168, 91–100. http://dx.doi.org/10.1016/j.jweia.2017.05.008, URL https://www.sciencedirect.com/science/article/pii/S0167610516306341.

Jafari, M., Hou, F., Abdelkefi, A., 2020. Wind-induced vibration of structural cables. Nonlinear Dynam. 100, 351–421.

King, R., 1977. A review of vortex shedding research and its application. Ocean Eng. 4 (3), 141–171. http://dx.doi.org/10.1016/0029-8018(77)90002-6, URL https://www.sciencedirect.com/science/article/pii/0029801877900026.

Komatsu, S., Kobayashi, H., 1980. Vortex-induced oscillation of bluff cylinders. J. Wind Eng. Ind. Aerodyn. 6 (3–4), 335–362.

Kwok, K., Wilhelm, P., Wilkie, B., 1988. Effect of edge configuration on wind-induced response of tall buildings. Eng. Struct. 10 (2), 135–140.

Lamb, S., Kwok, K.C.S., 2017. Sopite syndrome in wind-excited buildings: productivity and wellbeing impacts. Build. Res. Inf. 45, 347–358.

Lamberti, G., Amerio, L., Pomaranzi, G., Zasso, A., Gorlé, C., 2020. Comparison of high resolution pressure measurements on a high-rise building in a closed and open-section wind tunnel. J. Wind Eng. Ind. Aerodyn. 204, 104247. http://dx.doi.org/10.1016/j.jweia.2020.104247, URL https://www.sciencedirect.com/science/article/pii/S0167610520301574.

Mannini, C., Marra, A., Bartoli, G., 2014. VIV–galloping instability of rectangular cylinders: Review and new experiments. J. Wind Eng. Ind. Aerodyn. 132, 109–124.

Mannini, C., Marra, A.M., Bartoli, G., 2015. Experimental investigation on VIV-galloping interaction of a rectangular 3: 2 cylinder. Meccanica 50 (3), 841–853.

Marra, A.M., Mannini, C., Bartoli, G., 2015. Measurements and improved model of vortex-induced vibration for an elongated rectangular cylinder. J. Wind Eng. Ind. Aerodyn. 147, 358–367. http://dx.doi.org/10.1016/j.jweia.2015.08.007, URL https://www.sciencedirect.com/science/article/pii/S0167610515002123.

Matsumoto, M., 1996. Aerodynamic damping of prisms. J. Wind Eng. Ind. Aerodyn. 59 (2–3), 159–175.

Matsumoto, M., Kobayashi, Y., Shirato, H., 1996. The influence of aerodynamic derivatives on flutter. J. Wind Eng. Ind. Aerodyn. 60, 227–239.

Matsumoto, M., Mizuno, K., Okubo, K., Ito, Y., 2005. Torsional flutter and branch characteristics for 2-D rectangular cylinders. J. Fluids Struct. 21 (5–7), 597–608.

Matsumoto, M., Shiraishi, N., Shirato, H., Stoyanoff, S., Yagi, T., 1993. Mechanism of, and turbulence effect on vortex-induced oscillations for bridge box girders. J. Wind Eng. Ind. Aerodyn. 49 (1), 467–476. http://dx.doi.org/10.1016/0167-6105(93)90041-L, URL https://www.sciencedirect.com/science/article/pii/016761059390041L.

Matsumoto, M., Shirato, H., Mizuno, K., Shijo, R., Hikida, T., 2008. Flutter characteristics of H-shaped cylinders with various side-ratios and comparisons with characteristics of rectangular cylinders. J. Wind Eng. Ind. Aerodyn. 96 (6–7), 963–970.

Micheli, L., Hong, J., Laflamme, S., Alipour, A., 2020. Surrogate models for high performance control systems in wind-excited tall buildings. Appl. Soft Comput. 90, 106133. http://dx.doi.org/10.1016/j.asoc.2020.106133, URL https://www.sciencedirect.com/science/article/pii/S1568494620300739.

Micheli, L., Laflamme, S., Alipour, A., Cao, L., 2019. Life-cycle cost evaluation strategy for high-performance control systems under uncertainties. J. Eng. Mech. 146, http://dx.doi.org/10.1061/(ASCE)EM.1943-7889.0001711.

Nakamura, Y., Ohya, Y., Tsuruta, H., 1991. Experiments on vortex shedding from flat plates with square leading and trailing edges. J. Fluid Mech..

Nguyen, D.T., Hargreaves, D.M., Owen, J.S., 2018. Vortex-induced vibration of a 5:1 rectangular cylinder: A comparison of wind tunnel sectional model tests and computational simulations. J. Wind Eng. Ind. Aerodyn. 175, 1–16. http://dx.doi.org/10.1016/j.jweia.2018.01.029, URL https://www.sciencedirect.com/science/article/pii/S0167610517304890.

Noda, M., Utsunomiya, H., Nagao, F., Kanda, M., Shiraishi, N., 2003. Effects of oscillation amplitude on aerodynamic derivatives. J. Wind Eng. Ind. Aerodyn. 91 (1–2), 101–111.

Pantazopoulos, M.S., 1994. Vortex-induced vibration parameters: Critical review. URL https://www.osti.gov/biblio/55708.

Parkinson, G., 1989. Phenomena and modelling of flow-induced vibrations of bluff bodies. Prog. Aerosp. Sci. 26 (2), 169–224.

Pomaranzi, G., Amerio, L., Schito, P., Lamberti, G., Gorlé, C., Zasso, A., 2022a. Wind tunnel pressure data analysis for peak cladding load estimation on a high-rise building. J. Wind Eng. Ind. Aerodyn. 220, 104855. http://dx.doi.org/10.1016/j.jweia.2021.104855, URL https://www.sciencedirect.com/science/article/pii/S0167610521003299.

Pomaranzi, G., Bistoni, O., Schito, P., Rosa, L., Zasso, A., 2021. Wind effects on a permeable double skin façade, the ENI head office case study. Fluids 6 (11), 415.

Pomaranzi, G., Daniotti, N., Schito, P., Rosa, L., Zasso, A., 2020. Experimental assessment of the effects of a porous double skin façade system on cladding loads. J. Wind Eng. Ind. Aerodyn. 196, 104019. http://dx.doi.org/10.1016/j.jweia.2019.104019, URL https://www.sciencedirect.com/science/article/pii/S0167610519306191.

Pomaranzi, G., Pasqualotto, G., Zasso, A., et al., 2022b. Investigation of the effects due to a permeable double skin façade on the overall aerodynamics of a high-rise building. Wind Struct. 35 (3), 213–227.

Rishabh, R., Franklin, T., Austin, F., Bradley, S., William, F., 2019. Influence of architectural form on the crosswind response of tall buildings. In: The 15th International Conference on Wind Engineering Beijing. China.

Samali, B., Azad, A., Ngo, T., 2014. Control of wind-induced motion of mid-rise buildings using smart facade systems. In: Sixth World Conference on Structural Control and Monitoring: Proceedings of the 6th Edition of the World Conference of the International Association for Structural Control and Monitoring. IACSM, Held in Barcelona, Spain, 15-17 July 2014, pp. 2856–2863.

Sarpkaya, T., 2004. A critical review of the intrinsic nature of vortex-induced vibrations. J. Fluids Struct. 19 (4), 389–447. http://dx.doi.org/10.1016/j.jfluidstructs.2004.02.005, URL https://www.sciencedirect.com/science/article/pii/S0889974604000350.

Sharma, A., Mittal, H., Gairola, A., 2018. Mitigation of wind load on tall buildings through aerodynamic modifications. J. Build. Eng. 18, 180–194.

Shiraishi, N., Matsumoto, M., 1983. On classification of vortex-induced oscillation and its application for bridge structures. J. Wind Eng. Ind. Aerodyn. 14 (1–3), 419–430.

Tamura, T., Dias, P., 2003. Unstable aerodynamic phenomena around the resonant velocity of a rectangular cylinder with small side ratio. J. Wind Eng. Ind. Aerodyn. 91 (1–2), 127–138.

Tamura, T., Miyagi, T., 1999. The effect of turbulence on aerodynamic forces on a square cylinder with various corner shapes. J. Wind Eng. Ind. Aerodyn. 83 (1–3), 135–145.

Tang, Z., Zou, G., Li, L., 2024. The effect of damping on the vortex-induced vibration of a rectangular prism. Phys. Fluids 36 (2), http://dx.doi.org/10.1063/5.0188667, Cited by: 0; All Open Access, Bronze Open Access. URL https://www.scopus.com/inward/record.uri?eid=2-s2.0-85185004459&doi=10.1063%2f5.0188667&partnerID=40&md5=2842f8cd02922822b5bb036675279f76.

Teimourian, A., Teimourian, H., 2021. Vortex shedding suppression: A review on modified bluff bodies. Eng 2 (3), 325–339.

Vega, R.E., Konz, R.C., 2009. Cladding performance of high-rise buildings in the houston CBD during hurricane ike. In: Forensic Engineering 2009: Pathology of the Built Environment. pp. 739–748.

Wang, L., yan Fan, X., 2019. Failure cases of high chimneys: A review. Eng. Fail. Anal. 105, 1107–1117. http://dx.doi.org/10.1016/j.engfailanal.2019.07.032, URL https://www.sciencedirect.com/science/article/pii/S1350630719302833.

Williamson, C., Govardhan, R., 2008. A brief review of recent results in vortex-induced vibrations. J. Wind Eng. Ind. Aerodyn. 96 (6), 713–735. http://dx.doi.org/10.1016/j.jweia.2007.06.019, 5th International Colloquium on Bluff Body Aerodynamics and Applications, URL https://www.sciencedirect.com/science/article/pii/S0167610507001262.